1 2

# Pressure-driven distillation using air-trapping membranes for fast and selective water purification

4

5

3

**Authors:** Duong T. Nguyen<sup>1</sup>, Sangsuk Lee<sup>1</sup>, Kian P. Lopez<sup>2</sup>, Jongho Lee<sup>3</sup>, and Anthony P. Straub<sup>1,4</sup>\*

### Affiliations

- 6 Department of Civil, Environmental, and Architectural Engineering, University of Colorado
- 7 Boulder; Boulder, CO 80309, USA.
- <sup>2</sup> Department of Chemical and Biological Engineering, University of Colorado Boulder; Boulder,
- 9 CO 80309, USA.
- <sup>3</sup> Department of Civil Engineering, University of British Columbia; Vancouver, British
- 11 Columbia V6T 1Z4, Canada.
- <sup>4</sup> Materials Science and Engineering Program, University of Colorado Boulder; Boulder, CO
- 13 80309, USA.
- \*Corresponding author. Email: anthony.straub@colorado.edu

15 16

17

18

19

20

21

22

23

24

25

26

27

28

### Abstract

Membrane technologies that enable the efficient purification of impaired water sources are needed to address growing water scarcity. However, state-of-the-art engineered membranes are constrained by a universal, deleterious trade-off where membranes with high water permeability lack selectivity. Current membranes also poorly remove low molecular weight neutral solutes and are vulnerable to degradation from oxidants used in water treatment. We report a water desalination technology that uses applied pressure to drive vapor transport through membranes with an entrapped air layer. Since separation occurs due to a gas-liquid phase change, near-complete rejection of dissolved solutes including sodium chloride, boron, urea, and *N*-nitrosodimethylamine is observed. Membranes fabricated with sub-200 nm thick air layers showed water permeabilities that exceed those of commercial membranes without sacrificing salt rejection. We also find the air-trapping membranes tolerate exposure to chlorine and ozone oxidants. The results advance our understanding of evaporation behavior and facilitate high throughput ultraselective separations.

293031

#### Teaser

Water desalination is shown using vapor transport through membranes that trap nanoscale air bubbles.

3435

36

37 38

3940

### **MAIN TEXT**

## Introduction

Anthropogenic climate change and increasing water demands have led to more severe water scarcity, necessitating the use of non-traditional water sources including wastewater, seawater, and brackish water (I-3). Safe use of these sources requires water treatment systems that remove nearly all dissolved constituents from contaminated water. Membrane technologies, in particular reverse osmosis (RO), have emerged as the premier tools for water reuse and desalination due to their high energy efficiency, ease of operation, and compact design (4-6).

Despite their widespread implementation, RO systems have experienced longstanding limitations in performance related to the membrane materials. Current polymeric salt-rejecting membranes are constrained by a trade-off where high permeability comes at the cost of decreased water-salt selectivity (7, 8). Membranes also routinely fail to remove harmful contaminants since low molecular weight neutral species can pass through polymer membranes (9–11); contaminants that are poorly rejected by RO include boron, urea, *N*-nitrosodimethylamine (NDMA), and 1,4-dioxane. Furthermore, the polymeric materials used in RO membranes are vulnerable to chemical oxidation, decreasing longevity and precluding cleaning of the membranes with chlorine, ozone, and other disinfectants (12, 13).

The fundamental constraints of membranes used in current RO systems motivate the study of alternative separation processes for advanced water treatment. Distillation-based technologies, where separation relies on a gas-liquid phase change, have been used for millennia and maintain key advantages compared to RO. Since separation is accomplished via a phase change, distillation systems remove all low volatility species from water, including those poorly rejected by RO (14–16). Distillation technologies can also operate with feedwaters containing harsh oxidants, solvents, and other chemicals (17).

The principal drawback of distillation technologies is that they are driven by heat, resulting in high energy consumption associated with thermal losses in the system (18, 19). We therefore pursued the development of a water purification system where pressure, rather than heat, is used to drive a gas-liquid phase transition through a membrane. This pressure-driven distillation process can retain the high energy efficiency and small footprint of RO, but also achieve complete removal

of non-volatile species and tolerate harsh feedwaters (20). Pressure-driven distillation distinguishes itself from existing thermal membrane distillation since it does not require heat energy and is distinct from osmotic distillation, which requires a secondary separation step (21). The feasibility of desalination via pressure-driven distillation is evident from theory, but demonstration of the system has not been possible due to a lack of appropriate membranes for the process (22).

In this work, we present a proof-of-concept study on a separation technology that operates using pressure-driven distillation through air-trapping hydrophobic membranes. In this system, applied pressure results in a partial vapor pressure difference across a thin air gap, driving evaporation on the feed side of the membrane, gas-phase diffusion, and condensation on the permeate (Fig. 1A). Nanoporous membranes with sub-200 nm thick air layers were synthesized to probe transport and desalination performance. The membranes show near-complete rejection of low volatility contaminants, including dissolved salts and micropollutants. By decreasing the air layer thickness, high water permeabilities are demonstrated without sacrificing water-salt selectivity, showing the technology can circumvent the permeability-selectivity trade-off that constrains conventional membrane-based desalination systems. The use of an air layer as a separation barrier allows desalination performance to be maintained even when membranes are exposed to chlorine and ozone disinfectants.

### Results

# Pressure-driven distillation through nanoscale air gaps

Air-trapping membranes for proof-of-concept testing were fabricated using porous anodic aluminum oxide substrates modified with a controlled hydrophobic coating. The hydrophobic coating was confined to a sub-micron layer on the top surface of the membrane using sequential masking, metal sputtering, and hydrophobic coating with fluorinated alkyl silane (Fig. 1B). The resulting membranes exhibited a superhydrophobic top surface with a water contact angle of  $161.2\pm2.0^{\circ}$  and a hydrophilic bottom surface (Fig. 1C). The presence of fluorinated groups associated with the hydrophobic surface coating was confirmed by Fourier transform infrared spectroscopy and energy-dispersive X-ray spectroscopy (fig. S2 and S3). Scanning electron microscopy (SEM) revealed the membranes had uniform pore diameters of  $27.1\pm5.2$ ,  $43.3\pm15.4$ ,

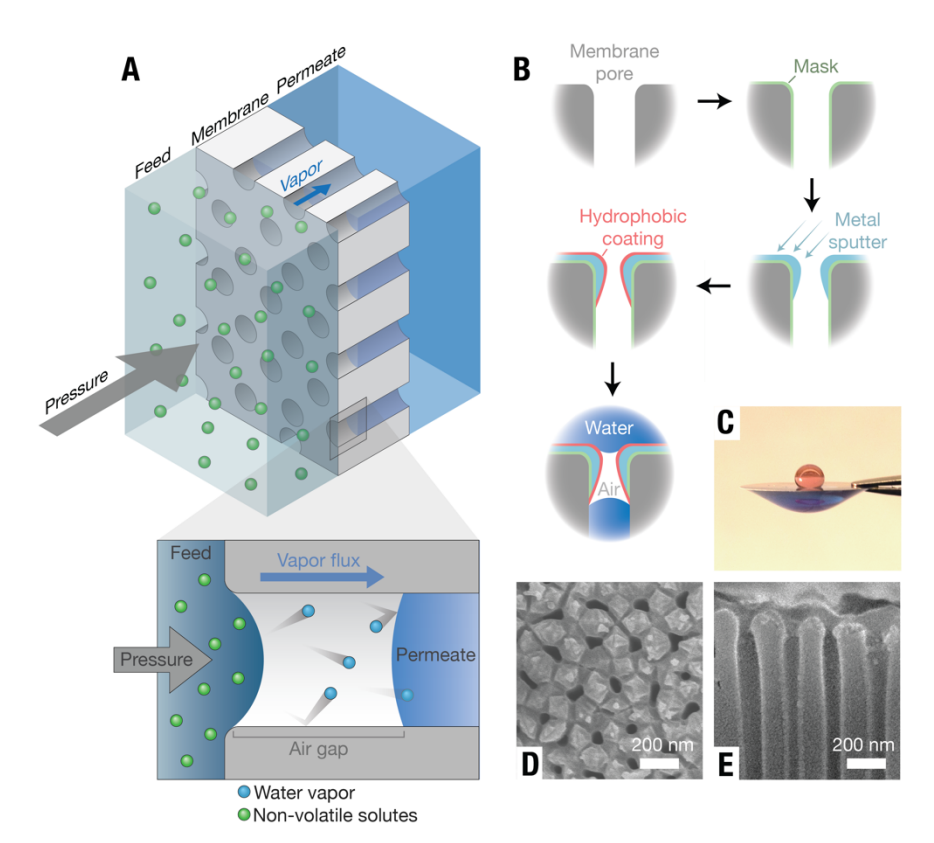


Figure 1 | Design of ultrathin air-trapping membranes for pressure-driven vapor transport.

(A) Schematic diagram of pressure-driven water vapor transport through a nanoporous membrane with an ultrathin air gap. (B) Schematic of the fabrication process: a porous alumina membrane is modified with a hydrophilic masking layer, sputtered with controlled metal deposition into pores, selectively coated with a hydrophobic layer on the metal surface, and treated to remove the residual masking layer. (C) Water contact angle on the top and bottom surfaces of the membrane. Scanning electron micrograph of the (D) top surface and (E) cross section of the upper surface of the membrane.

or  $75.5\pm14.9$  nm depending on the pore size of the initial porous alumina substrate (Fig. 1D, E and fig. S4). SEM detection of backscattered electrons confirmed that the hydrophobic metal layer on the top surface of the membrane could be varied between thicknesses of  $119.0\pm12.7$  nm and  $189.3\pm34.8$  nm based on the sputtering angle (fig. S5). For comparison, membranes with hydrophobic layers spanning the entire membrane thickness (approximately 50  $\mu$ m) were also fabricated.

Air-trapping membranes have not been previously used in pressurized applications because liquid water can enter the pores when small hydraulic pressures (3–5 bar) are applied, compromising water-salt selectivity (table S1). We found that the sub-100 nm pore size

hydrophobic membranes resist wetting at high hydraulic pressures and demonstrate pressure-driven water vapor flow that increases with increasing hydraulic pressure (Fig. 2A). For 75.5±14.9 nm pore size membrane, the water flux increased monotonically with pressure, reaching normalized fluxes up to 88.0 kg m<sup>-2</sup>h<sup>-1</sup> at pressures of 12.1 bar. Removal experiments for Allura Red AC dye (496 g/mol, Stokes diameter of approximately 1 nm) over 24 h quantified using UV-Vis absorbance showed that permeate samples had identical spectra as DI water in the measured wavelength range (300 to 800 nm), indicating more than 99.99% dye removal (Fig. 2B). Salt rejection experiments with a 50 mM sodium chloride feed solution measured for a 24-hour period observed rejections higher than 99.8%, and permeate samples had electrical conductivities approaching those of DI water (Fig. 2C). Long-term experiments over a 7-day period found that salt rejection and water flux rates could be maintained in fabricated membranes (fig. S8). Water flux measurements were consistent with transport models based on water evaporation rates and Maxwell-Stefan diffusion theory. Simulated water fluxes using membrane properties (e.g., pore size, thickness, porosity) determined via SEM without fitting parameters showed less than 15% deviation from experimental measurements (fig. S7).

Decreasing the pore sizes of the membrane allowed for operation a higher hydraulic pressure without pore wetting (Fig. 2D). The liquid entry pressure (LEP) describes the pressure at which an air layer can no longer be maintained in a hydrophobic membrane. The measured LEPs of membranes with pore sizes of 75.5±14.9, 43.3±15.4, and 27.1±5.2 nm were 12.1±1.7, 20.8±3.5, and 48.3±5.2 bar, respectively. These maximum pressures were aligned with predictions based on the Young-Laplace equation, and we therefore expect that higher operating pressures will be possible by further decreasing the membrane pore size. The LEP of 48.3±5.2 bar measured for the 27.1±5.2 nm pore size membrane was more than a factor of ten higher than previous air-trapping desalination membranes and appropriate for treating seawater (typical osmotic pressure of 28 bar) (23, 24).

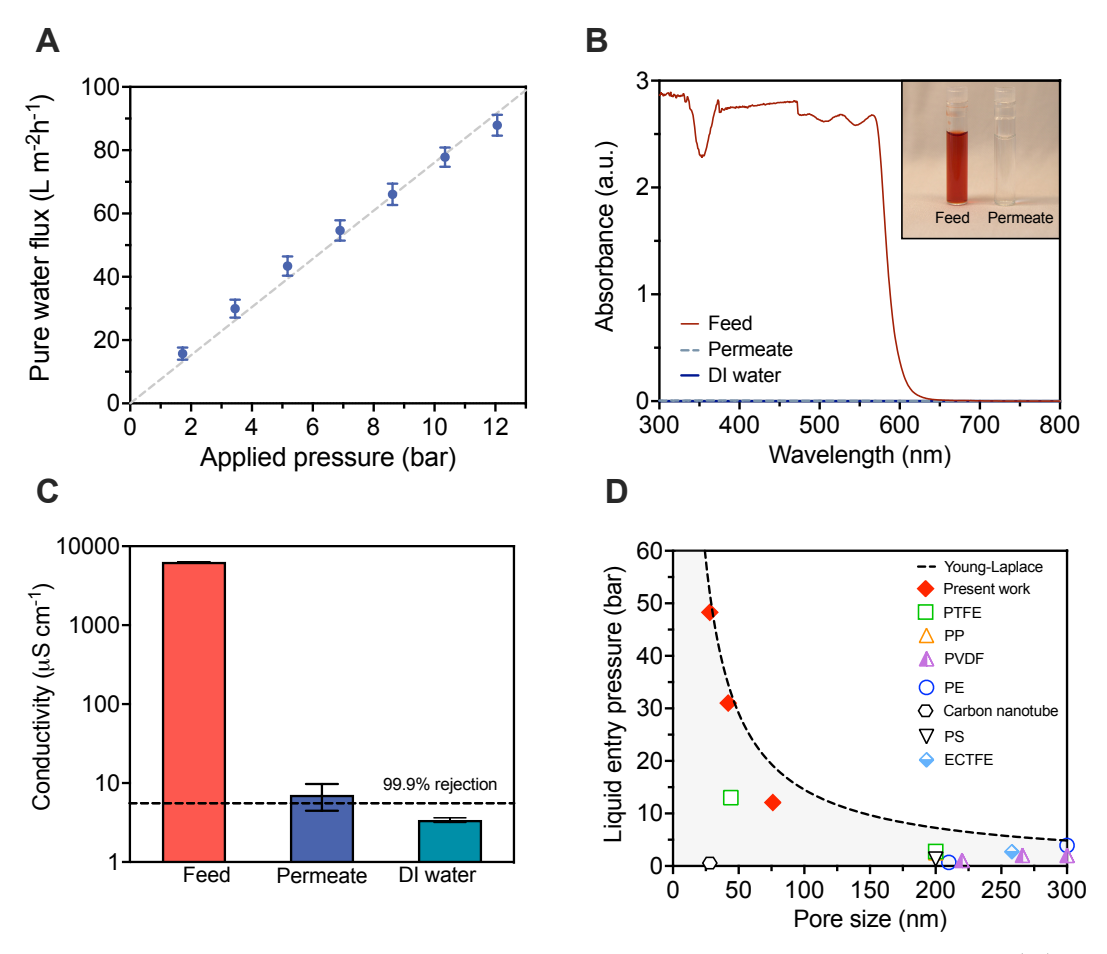


Figure 2 | Desalination performance of ultrathin air-trapping membranes. (A) Measured water flux as a function of applied hydraulic pressure for 75.5±14.9 nm pore size membranes with a 189 nm thick hydrophobic layer. Water flux is normalized to the active pore area of the membrane based on a surface porosity of 14.5%. Feed solution was DI water, temperature was 60 °C, and hydraulic pressures varied from 1.72 to 12.06 bar. The dashed line is a linear fit to guide the eye. (B) UV-Vis spectra for 1 mM Allura Red dye feed water, permeate water, and deionized (DI) water. The inset photo shows the feed and permeate samples. (C) Measured conductivities of the feed, permeate, and DI water for desalination of a 50 mM NaCl solution. The black dashed line depicts 99.9% salt rejection. The operating pressure and temperature were 10.34 bar and 60 °C, respectively. (D) Liquid entry pressure as a function of pore size for the membranes fabricated in this work and membranes reported in the literature: commercial membranes made of polytetrafluoroethylene (PTFE), polyvinylidene fluoride (PVDF), polypropylene (PP), and polyethylene (PE) and fabricated membranes made of carbon nanotubes, nanofibrous polystyrene (PS), and poly(ethylene chlorotrifluoroethylene) (ECTFE)(25–30). The dashed curve presents theoretical values obtained from the Young-Laplace equation with an intrinsic contact angle of  $120^{\circ}$ . In all plots, error bars denote  $\pm 1$  SD around the mean from three separate membranes.

# Achievable water permeability and salt rejection

State-of-the-art membranes are subject to a trade-off between water permeability and water-salt selectivity where a gain in water permeability results in a loss in salt rejection (31, 32). In contrast, we observed membranes that rely on a gas-liquid phase change can increase permeability without sacrificing water-salt selectivity by decreasing the thickness of the air layer. We show shortening the air layer thickness to 119.0±12.7 allows for the water permeability of the entrapped air layer (that is, the permeability normalized the active pore area) to reach values up to 8.9 kg m<sup>-2</sup>h<sup>-1</sup>bar<sup>-1</sup> while maintaining greater than 99% salt rejection (Fig. 3A). Since the membranes have a surface porosity of 14.5%, the water permeability normalized to the total membrane area is 1.3 kg m<sup>-2</sup>h<sup>-</sup> <sup>1</sup>bar<sup>-1</sup>. The lack of a measurable change in salt rejection as the thickness decreased was consistent with our understanding that selectivity in the air-trapping membranes is attributable to the gasliquid phase change transport mechanism. Due to their low thickness, the water permeabilities of membranes in this work were notably higher than previous work in osmotic and membrane distillation systems, where membrane are tens of microns thick and generally have water permeabilities 1–2 orders of magnitude lower (21). While the aim of this study was not to produce membranes that outcompete commercial RO membranes in terms of water permeability, our measurements provide experimental evidence that it is possible for air-trapping membranes to reach the water permeabilities needed for efficient water desalination (33).

The high water permeabilities observed in this study are particularly revealing because the fabricated membranes approach the minimum air layer thickness derived from thermodynamic wetting theory (34, 35). Pore wetting is thermodynamically unfavorable when the grand potential of the wetted state is greater than the grand potential of the unwetted air-filled state. As the aspect ratio of the hydrophobic pore decreases (that is, as the air layer becomes thinner), spontaneous pore wetting due to capillary condensation becomes more favorable. For the 75.5 nm diameter pores studied in this work, the minimum predicted thickness for the air layer is 116.8 nm, assuming an intrinsic water contact angle of 120°. In our testing, water permeability could be measured for membranes with a thickness down to 119.0 nm, and membranes with a thinner hydrophobic layer showed spontaneous pore wetting. Our measurements therefore showed good agreement with theory, and provide experimental support for two-decades old predictions on the minimum thickness of a hydrophobic pore (34, 35). Since the pores here approach the minimum possible

aspect ratio, the observed water permeabilities may be near the upper limit possible using a vapor transport through an air-filled pore (22).

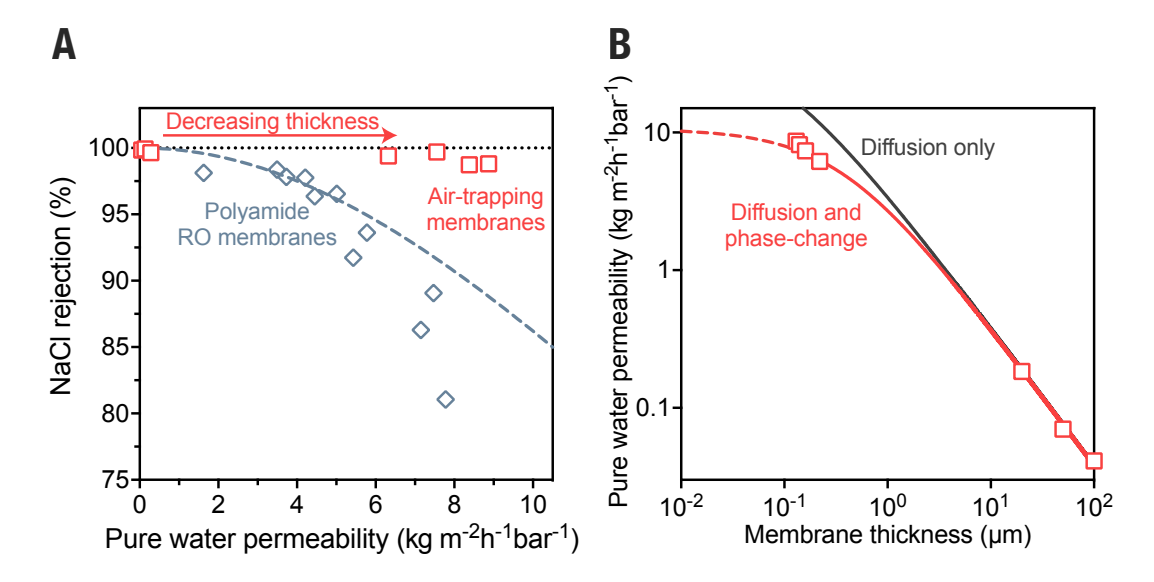


Figure 3 | Achievable water permeability in air-trapping membranes. (A) Normalized pure water permeability and sodium chloride rejection of air-trapping membranes (red squares). The permeability of air-trapping membranes was increased by decreasing the thickness of the air layer from 100 μm to 119 nm. Permeability values of air-trapping membranes are normalized to the active pore area based on a surface porosity of 14.5%. Membranes were tested with 50 mM NaCl at a temperature of 60 °C and an applied pressure of 10.34 bar. For comparison, the permeability-selectivity trade-off curve for polyamide membranes is shown (blue diamonds and dotted blue line). (B) Water permeability of air-trapping membranes as a function of membrane thickness (red squares). Simulated curves based on only diffusion resistances or diffusion and phase-change resistances are shown. Phase-change resistances were modeled using a condensation coefficient of 0.33. Dashed lines indicate thicknesses below the minimum thickness that causes pore wetting.

Latent heat transfer by water molecules traveling through the entrapped air layer was found to have a negligible impact on the water flux. Evaporation on the feed air-liquid interface and condensation on the permeate air-liquid interface result in cooling and heating, respectively, due to latent heat transfer through the membrane. However, conductive heat transfer through the ultrathin air layer and the membrane material transfers heat back to the feed stream, mitigating the buildup of a temperature difference. Therefore, no temperature difference across the membrane was observed in any of our tests, and theoretical simulations showed that the system operates in

near isothermal conditions with a temperature difference across the membrane less than  $1 \times 10^{-3}$  °C (fig. S10 and S11). Since temperature effects in the process are negligible, we expect that the energy efficiency of pressure-driven distillation will be similar to that of reverse osmosis since both processes are driven by hydraulic pressure and offer comparable water fluxes (20).

Decreasing the air layer thickness to less than 200 nm causes transport to occur in a regime where vapor permeability is limited by resistances associated with evaporation and condensation rather than diffusion resistances (34). For membranes with high vapor layer thicknesses (20–100 μm), we found that transport theory based on only diffusion resistances showed good agreement with measured water permeabilities (Fig. 3B). However, when the vapor layer thickness decreased to below 200 nm, water permeability values were lower than those predicted using only diffusion resistances, indicating substantial contributions from resistances at the liquid-vapor interface. The resistances caused by the phase change are described by the condensation coefficient,  $\sigma$ , a fundamental property which quantifies the probability that an incident vapor molecule condenses at the vapor-liquid interface (36). The condensation coefficient has been difficult to probe experimentally, and measured values have varied two orders of magnitude due to major uncertainties related to temperature, interface area, and salinity (37). Calculations based on our experimental measurements found that the condensation coefficient at 0.68 bar and 60 °C was 0.27 in agreement with a previous study using air-trapping membranes (36). Our ability to estimate the condensation coefficient demonstrates the utility of air-trapping membranes as a platform to study gas-liquid phase-change phenomena, and further work may be able to accurately measure this coefficient in a variety of experimental conditions.

# Solute rejection and chemical resilience

Using a vapor layer as a separation barrier results in fundamentally different selective properties as compared to conventional RO membranes that use a thin polymer film. Air-trapping membranes were evaluated for the removal of three contaminants poorly rejected by commercial polyamide RO membranes: boron, urea, and NDMA (10, 33). The solution pH for each contaminant was adjusted to below the pKa to ensure that undissociated species were dominant in the feed water. The air-trapping membranes demonstrated 99.1% and 98.1% rejection of boron and urea, respectively, indicating near-complete removal of both solutes (Fig. 4A). In contrast, polyamide RO membranes poorly rejected boron and urea with 45.5% and 35.6% rejection, respectively.

Rejection of NDMA in the fabricated air-trapping membranes was 95.8% due to the slight volatility of NDMA but still exceeded the 43.4% rejection observed with polyamide RO membranes. The high rejections are consistent with our understanding of the air layer acting as a near-impermeable separation barrier for non-volatile solutes (16, 24, 38).

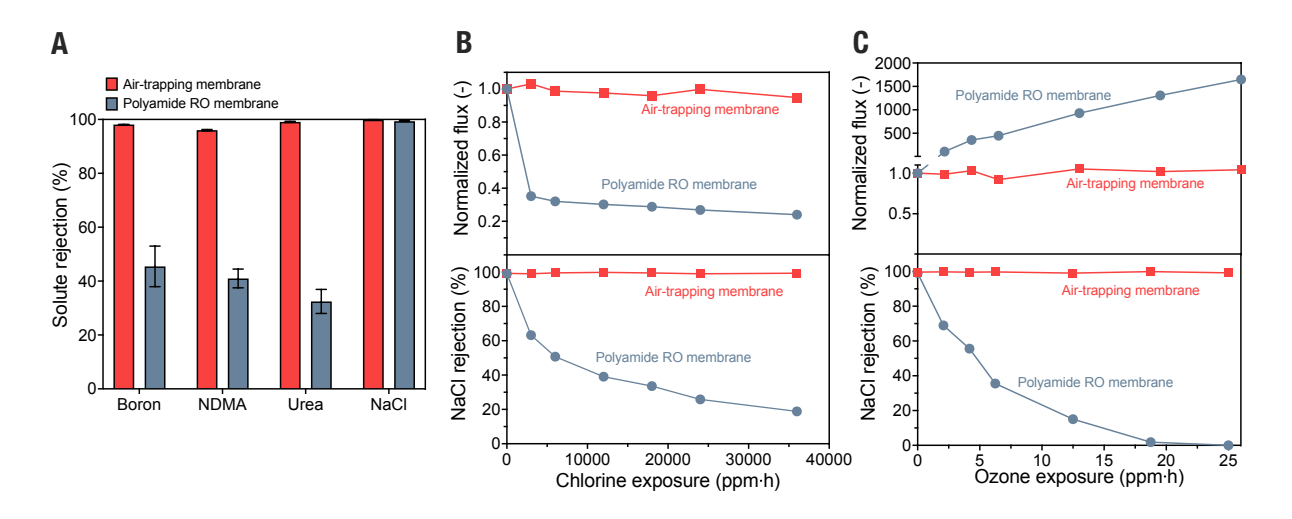


Figure 4 | Selectivity and oxidation resistance of fabricated membranes. (A) Rejection of boron, *N*-nitrosodimethylamine (NDMA), urea, and sodium chloride by the fabricated air-trapping membranes with a pore size of 75.5±14.9 nm and commercial polyamide RO membranes (Dow SW30). Error bars indicate SD for duplicate experiments using two membranes fabricated in the same procedure. (B) Effect of chlorine exposure on the water flux and salt rejection of the fabricated air-trapping membranes and polyamide RO membranes. Chlorine concentration is 1000 ppm at pH 4, and exposure time varies from 1 to 36 h. (C) Effect of ozone exposure on membrane water flux and salt rejection. Ozone concentration is 25 ppm at pH 7, and exposure time varies from 0.083 to 1 h. The applied hydraulic pressure was fixed at 10.3 bar for all experiments.

Separations with an entrapped air layer enable the use of oxidation-resistant hydrophobic membrane materials. Desalination experiments were conducted with fabricated membranes after exposures to high doses of chlorine and ozone, two strong oxidants used in water treatment processes (Fig. 4B, C) (12). After chlorine exposure of 36,000 ppm h at pH 4 (1000 ppm for 36 h) or ozone exposure of 25 ppm h at pH 7 (25 ppm for 1 h), the membranes demonstrated greater than 99% NaCl rejection and less than 6% variation in water flux. Conversely, polyamide RO membranes exposed to chlorine and ozone showed less than 20% salt rejection and severe changes

in the water flux. The unchanged structure and chemistry of the fabricated membranes after oxidative exposure were confirmed using SEM, FTIR, and contact angle analysis (fig S1, S2, and S4).

#### Discussion

We have demonstrated a pressure-driven distillation process for water purification that uses applied pressure to drive vapor flow through an air-trapping membrane. Proof-of-concept experiments found that such membranes can achieve high rejection (greater than 99%) of non-volatile solutes including sodium chloride, boron, and urea. Membranes with a 27.1 nm pore diameter were found to operate at pressures up to 48.3 bar. By decreasing the thickness of the air layer to 119.0 nm, we find that normalized permeabilities of up 8.9 kg m<sup>-2</sup>h<sup>-1</sup>bar<sup>-1</sup> can be achieved without sacrificing salt rejection. We also find that the performance of air-trapping membranes is unaffected by exposure to sustained high concentrations of chlorine and ozone.

Since the desalination approach presented here relies on using an applied pressure to drive flow through a semi-permeable membrane, we expect that air-trapping membranes can be substituted directly for conventional RO membranes with the potential advantages of improved permeability, selectivity, and oxidation resistance. In desalination applications, the high selectivity of air-trapping membranes towards non-volatile solutes may obviate the costly secondary treatment processes currently needed to remove boron since relatively low concentrations of the contaminant (0.5–1 mg L<sup>-1</sup>) can harm agriculture (*39*). For water reuse applications, high removal of NDMA, urea, and other contaminants may improve the safety of product water and reduce the need for further downstream processes (*10*). We also envision the high selectivity of the air-trapping membrane may allow for more efficient ultrapure water production and water recycling in space applications (*40*).

A key advantage of pressure-driven distillation is that it can potentially use a variety of membrane materials and structures to achieve the required air-trapping structure, allowing for more tailored and chemically robust water treatment systems than conventional salt rejecting membranes that rely on polyamide or cellulose acetate chemistry. Here, we find that fabricated hydrophobic alumina membranes resist damage from chemical oxidants such as chlorine and ozone. We expect that other more scalable materials, including hydrophobic polymers, can be

developed for the process and offer similar resistance to chemical oxidation (6, 17, 41, 42). The ability to use free chlorine or ozone, rather than chloramines, in treatment trains can prevent the formation of certain harmful disinfection byproducts such as NDMA (43). Strong oxidants like chlorine and ozone also inhibit fouling associated with organic and biological matter, providing potentially transformative improvements in water treatment performance and membrane longevity (12).

Continued investigations are needed to address challenges of pressure-driven distillation related to wetting, fouling, and scale-up. Air-trapping membrane are vulnerable to wetting from low surface tension liquids and foulants, and further work is needed to comprehensively identify fouling behavior. Development efforts are also required to fabricate scalable large-area hydrophobic porous membranes. Future membranes should have small monodisperse pore sizes to operate at high applied pressure without wetting and use thin air layers to maximize permeability while avoiding trade-offs associated with membrane wetting (44). Membranes should also have high surface porosities to maximize the achievable active membrane area. Tailored structures that have already shown promise in related membrane distillation processes, such as omniphobic or Janus designs, may also offer the potential for most robust separations (45).

Although this work has laid out the fundamental principles of pressure-driven distillation technology, key knowledge gaps exist related to interfacial and evaporation phenomena that underlie the process. In this study, we fabricated membranes with air layers that approached the minimum thickness possible based on thermodynamic models (35). We also experimentally detected interfacial resistances related to molecular reflection at the gas-liquid interface. Continued work is needed to establish a complete theoretical framework for transport in air-filled nanopores and identify the importance of interfacial resistances, nanoconfinement, cluster evaporation, and other behaviors that have been hypothesized in the literature (46, 47). We therefore anticipate that the membranes in this work can serve as a platform to study broadly important interfacial and evaporation phenomena.

### **Materials and Methods**

282

283

284

285

286

287

288

289

290

291

292

293

294

295

296

297

298299

300

301

302

303

304

305

306

307

308

309

310

311

312

## Fabrication of membranes with an ultrathin hydrophobic layer

Membranes with an ultrathin hydrophobic layer were fabricated using flat-sheet anodic aluminum oxide (AAO) membranes with varying pore diameters (27.1, 43.3, and 75.5 nm), a thickness of 50 μm, and a macroscopic diameter of 13 mm as the substrates (InRedox, CO, USA). The substrates were sandwiched between polished alumina plates to prevent deformation and annealed at 1000 °C for 2 h. The polycrystalline membranes were then exposed to the vapor of 3-aminopropyl triethoxysilane (Sigma-Aldrich, MO, USA) at a temperature of 70 °C and a vacuum pressure of 20 MPa for 4 h to create a hydrophilic layer of amine groups that would mask subsequent silanebased surface modification. Platinum was then deposited on the membranes using a magnetron sputter coater (Leica ACE600, Germany) with varying incident angles of 55° to 75° using argon as sputtering gas under a target-substrate distance 50 mm and a current of 35 mA. The incident angle is the angle at which the sputter approaches the membrane, an incident angle of 90° would be perpendicular to the membrane surface. The penetration depth inside alumina nanopores was tailored using geometric calculations verified with imaging and experimental measurements. Platinum-deposited membranes were then exposed to a hydrophobic grafting chemical, (heptadecafluoro-1,1,2,2-tetrahydrodecyl) triethoxysilane (Gelest Inc., PA, USA) at 90 °C for 12 h with a vacuum pressure of 20 MPa to selectively functionalize the platinum layer. The resulting membranes were floated on the interface of a mixture of 20% tetrabutylammonium fluoride/water (Fisher Scientific, MA, USA) for 30 min to remove the hydrophilic aminosilane layer. The membranes were finally rinsed with ultrapure water several times, dried with nitrogen gas, and placed under vacuum at 120 °C for 2 h.

Membranes with a thick hydrophobic layer were fabricated by coating the entire thickness of AAO with hydrophobic chemicals. These thicker membranes were used in some desalination testing and to validate models for transport. AAO membranes were annealed at 1000 °C for 2 h and then immersed in 30% H<sub>2</sub>O<sub>2</sub> solution (Fisher Scientific, MA, USA) at 120 °C for 30 min and thoroughly dried at 120 °C for 1 h and under nitrogen gas. (Heptadecafluoro-1,1,2,2-tetrahydrodecyl) triethoxysilane was grafted on the resulting membranes via vapor deposition in a vacuum oven at 120 °C for 3 h under a vacuum pressure of 20 MPa. The modified membranes were rinsed with ultrapure water, dried with nitrogen gas, and heated at 120 °C for 2 h.

### Material characterizations of the fabricated membranes

Membrane hydrophobicity was evaluated via water contact angle measurements with a calibrated tensiometer (Biolin Scientific, AZ, USA) using the sessile drop method with one water droplet of 20 μL. The top surface and cross-section of the membranes were imaged by field emission scanning electron microscopy (FESEM) using secondary and backscattered electron detectors (JEOL, Tokyo, Japan). Membrane samples were coated with 5 nm of carbon thread before taking images. The average pore size, porosity, and thickness of the membranes were extracted from FESEM images at various locations using Image J software (National Institute of Health, MD, USA). Five SEM images from similarly fabricated alumina membranes were used for ImageJ analysis and the surface pore size was considered to be the longest distance between two points on the pore boundaries (or the Feret's diameter). Elemental compositions of the membranes were quantified using an energy-dispersive X-ray spectroscopy (EDS) detector (Oxford Instruments, Oxfordshire, UK) coupled with the FESEM system operating at an accelerating voltage of 15 kV. Fourier transform infrared spectroscopy (FTIR) was conducted using a spectrometer with a diamond attenuated total reflection module (Cary 630, CO, USA).

# Measurement of water flux and solute rejection

Transport characterization was conducted using a membrane flow cell immersed in a DI water bath with regulating temperature and varying hydraulic pressure applied using a nitrogen gas cylinder (fig. S12). The test cell and adjacent tubing were immersed in a DI water bath with regulated temperature. Before each experiment, the test cell, feed channel, and permeate channel were cleaned by ultrapure water several times until less than 1 µS cm<sup>-1</sup> conductivity was detected when passing DI water through the feed and permeate tubes. The membranes with a 13 mm diameter were placed inside the cell and tightly sealed with fitted rubber O-rings. The feed channel was filled with water containing a solute (NaCl, boron, urea, or NDMA) and the permeate channel was filled with DI water to enable the condensation of water vapor. Measurements were only recorded when pressure and thermal equilibrium of the system had been reached after 4 h.

Water flux was determined by precisely monitoring the volume of water gained in the permeate tube and confirmed with the loss in volume of the feed. A digital camera with high resolution was set up to acquire images of the feed and permeate tubes to monitor water level changes as a function of time (Logitech C390s, CA, USA). NaCl concentration was measured using a calibrated conductivity meter (Oakton CON2700, MA, USA) and corrected for dilution in the permeate tube. Allura dye concentration was analyzed via its absorbance at 500 nm by a UV-Vis

spectrophotometer (Hach DR6000, CO, USA). Urea concentration was quantified using a colorimetric method of urea and diacetyl monoxime allowing the detection limit down to 100 nM (48). Boron concentration was analyzed by inductively coupled plasma mass spectroscopy (ICP-MS) with a detection limit of 0.241 µg/L (49). NDMA concentration was measured by high performance liquid chromatography (HPLC) equipped with a C18 column using a mobile phase of ultrapure water/methanol with a ratio of 90:10 running at a flow rate of 1 mL min<sup>-1</sup> (50).

### Theoretical modeling of membrane performance

- The transport of a multi-component gas mixture (water vapor and air) through a porous medium was simulated using the Dusty-Gas Model, an extension of Stefan-Maxwell diffusion theory. This model has been experimentally corroborated in binary and ternary gas systems for diffusion of inert gases under uniform pressure from the Knudsen to molecular diffusion regime and thus is applicable to model our system (34, 51). A recent numerical study has found that the Dusty-Gas Model is valid even for very low aspect ratio pores such as those used in this study (52).
- Transport of water across a pore can be described by relating the vapor pressure to the maximum theoretical mass flux from an interface, *S*, by the Hertz hypothesis (*53*):

$$S = \sqrt{\frac{M}{2\pi R_g}} \frac{P_v}{\sqrt{T}} \tag{1}$$

where M is molar mass,  $R_g$  is the universal gas constant,  $P_v$  is partial vapor pressure, and T is temperature. This expression can be used to find the difference in evaporation rates at both ends of the pore,  $\Delta S$ , and can be further simplified by assuming an isothermal condition across the airgap:

$$\Delta S = \sqrt{\frac{M}{2\pi R_g}} \left( \frac{P_{v,f}}{\sqrt{T_f}} - \frac{P_{v,p}}{\sqrt{T_p}} \right) \cong \sqrt{\frac{M}{2\pi R_g T}} \Delta P_v \qquad (2)$$

where  $P_{v,f}$  and  $P_{v,p}$  are the partial vapor pressures at the feed and permeate sides of the pore, respectively, and  $T_f$  and  $T_p$  are the temperatures at the feed and permeate sides of the pores, respectively. Water mass flux across the membrane  $(J_w)$  can then be expressed as the product of membrane porosity,  $\varepsilon$ , and the difference in evaporation rate, divided by the total resistances experienced as water traverses the pore:

$$J_w = \varepsilon \frac{\Delta S}{\Sigma R} \cong \varepsilon \sqrt{\frac{M}{2\pi R_g T}} \left( \frac{1}{R_t} + \frac{1}{R_{i,f}} + \frac{1}{R_{i,p}} \right)^{-1} \Delta P_v = B_w \Delta P_v$$
 (3)

 $\sum R$  is the sum of multiple mass transport resistances where  $R_t$  corresponds to the transmission resistances, and  $R_{i,f}$  and  $R_{i,p}$  correspond to the interfacial resistances that occur on the feed and

permeate sides of the membrane, respectively.  $B_w$  is the vapor permeability coefficient, a proportionality factor which relates flux to a partial vapor pressure difference includes contributions from both transmission and interfacial resistances.

The water flux defined by Equation 3 is directly proportional to the vapor pressure difference across the membrane. From Raoult's law and the Kelvin equation, the water vapor pressure as a function of temperature concentration, and hydraulic pressure can be expressed as:

379 
$$P_{v}(T,C,P_{h}) = P_{v,0}(T)a_{w}(C)\exp\left(\frac{P_{h}V_{m}}{R_{g}T}\right) = P_{v,0}(T)\exp\left(\frac{(P_{h}-\pi)V_{m}}{R_{g}T}\right)$$
(4)

- where  $P_h$  is the hydraulic pressure relative to the ambient pressure, and  $V_m$  is the molar volume of
- liquid water. The water activity,  $a_w(C)$ , can be related to the osmotic pressure as follows  $\pi =$
- $-\frac{R_g T}{V_m} \ln a_w(C)$  to obtain the second expression in Equation 4. The equilibrium vapor pressure as a
- function of temperature,  $P_{\nu,0}(T)$ , can be calculated using the Antione equation:

$$P_{\nu,0}(T) = 10^{A - \frac{B}{C + T}} \tag{5}$$

where A, B, and C are the Antione constants for water.

Combining Equations 4 and 5, the overall water mass flux across the membrane can be expressed as follows:

388 
$$J_{w} = B_{w} \left[ P_{v} \left( T_{f,m}, C_{f,m}, P_{h,f} \right) - P_{v} \left( T_{p,m}, C_{p,m}, 0 \right) \right] \cong B_{w} \frac{P_{v,0}(T)V_{m}}{R_{a}T} \left( \Delta P - \Delta \pi \right)$$
 (6)

where  $T_{f,m}$  and  $T_{p,m}$  are temperatures at the membrane surface on the feed and permeate, respectively;  $C_{f,m}$  and  $C_{p,m}$  are the concentrations at the membrane surface on the feed and permeate, respectively;  $P_{h,f}$  is the applied hydraulic pressure on the feed side of the membrane; and the permeate side of the membrane is assumed to be at ambient pressure. Assuming isothermal conditions and applied pressures less than 100 bar, this equation can be further simplified so that the vapor pressure difference and water flux are linearly dependent on hydraulic and osmotic pressures (22). All simulations of water flux in this work solved the non-linear system of equations above and accounted for concentration polarization, heat transport, and temperature polarization; isothermal conditions are only assumed in the above definition to provide simplified explanations. Full descriptions of the calculations for mass transfer resistance, heat transfer, and concentration polarization are given in the Supplementary Materials.

### **References and Notes**

- 400 1. A. A. Uliana, N. T. Bui, J. Kamcev, M. K. Taylor, J. J. Urban, J. R. Long, Ion-capture electrodialysis using multifunctional adsorptive membranes. *Science*. **372**, 296–299 (2021).
- 402 2. M. Elimelech, W. A. Phillip, The Future of Seawater Desalination: Energy, Technology, and the Environment. *Science*. **333**, 712–717 (2011).
- 404 3. D. Hou, T. Li, X. Chen, S. He, J. Dai, S. A. Mofid, D. Hou, A. Iddya, D. Jassby, R. Yang, L. Hu, Z. J. Ren, Hydrophobic nanostructured wood membrane for thermally efficient distillation. *Sci. Adv.* 5, eaaw3203 (2019).
- 407 4. K. Zuo, W. Wang, A. Deshmukh, S. Jia, H. Guo, R. Xin, M. Elimelech, P. M. Ajayan, J. Lou, Q. Li, Multifunctional nanocoated membranes for high-rate electrothermal desalination of hypersaline waters. *Nat. Nanotechnol.* **15**, 1025–1032 (2020).
- 5. J. R. Werber, C. O. Osuji, M. Elimelech, Materials for next-generation desalination and water purification membranes. *Nat. Rev. Mater.* **1**, 1–15 (2016).
- 6. S. Ling, Z. Qin, W. Huang, S. Cao, D. L. Kaplan, M. J. Buehler, Design and function of biomimetic multilayer water purification membranes. *Sci. Adv.* **3**, e1601939 (2017).
- 414 7. H. B. Park, J. Kamcev, L. M. Robeson, M. Elimelech, B. D. Freeman, Maximizing the right 415 stuff: The trade-off between membrane permeability and selectivity. *Science*. **356**, 416 eaab0530 (2017).
- T. E. Culp, B. Khara, K. P. Brickey, M. Geitner, T. J. Zimudzi, J. D. Wilbur, S. D. Jons, A.
  Roy, M. Paul, B. Ganapathysubramanian, A. L. Zydney, M. Kumar, E. D. Gomez,
  Nanoscale control of internal inhomogeneity enhances water transport in desalination
- 420 membranes. *Science*. **371**, 72–75 (2021).
- 9. M. R. Chowdhury, J. Steffes, B. D. Huey, J. R. McCutcheon, 3D printed polyamide membranes for desalination. *Science*. **361**, 682–686 (2018).
- 423 10. Y. Wen, R. Dai, X. Li, X. Zhang, X. Cao, Z. Wu, S. Lin, C. Y. Tang, Z. Wang, Metal-424 organic framework enables ultraselective polyamide membrane for desalination and water 425 reuse. *Sci. Adv.* **8**, eabm4149 (2022).
- M. Di Vincenzo, A. Tiraferri, V.-E. Musteata, S. Chisca, R. Sougrat, L.-B. Huang, S. P.
  Nunes, M. Barboiu, Biomimetic artificial water channel membranes for enhanced desalination. *Nat. Nanotechnol.* 16, 190–196 (2021).
- 429 12. Y. Yao, P. Zhang, C. Jiang, R. M. DuChanois, X. Zhang, M. Elimelech, High performance 430 polyester reverse osmosis desalination membrane with chlorine resistance. *Nat. Sustain.* **4**, 431 138–146 (2021).
- 432 13. K. L. Cho, A. J. Hill, F. Caruso, S. E. Kentish, Chlorine Resistant Glutaraldehyde
  433 Crosslinked Polyelectrolyte Multilayer Membranes for Desalination. *Adv. Mater.* 27, 2791–
  434 2796 (2015).

- 14. S. Zhao, C. Jiang, J. Fan, S. Hong, P. Mei, R. Yao, Y. Liu, S. Zhang, H. Li, H. Zhang, C.
- Sun, Z. Guo, P. Shao, Y. Zhu, J. Zhang, L. Guo, Y. Ma, J. Zhang, X. Feng, F. Wang, H.
- Wu, B. Wang, Hydrophilicity gradient in covalent organic frameworks for membrane
- 438 distillation. *Nat. Mater.* **20**, 1551–1558 (2021).
- 439 15. A. V. Dudchenko, C. Chen, A. Cardenas, J. Rolf, D. Jassby, Frequency-dependent stability
- of CNT Joule heaters in ionizable media and desalination processes. *Nat. Nanotechnol.* 12,
- 441 557–563 (2017).
- 16. M. Wang, P. Zhang, X. Liang, J. Zhao, Y. Liu, Y. Cao, H. Wang, Y. Chen, Z. Zhang, F.
- Pan, Z. Zhang, Z. Jiang, Ultrafast seawater desalination with covalent organic framework
- membranes. *Nat. Sustain.* **5**, 518–526 (2022).
- 17. Y. Zhang, P. Zhao, J. Li, D. Hou, J. Wang, H. Liu, A hybrid process combining
- homogeneous catalytic ozonation and membrane distillation for wastewater treatment.
- 447 *Chemosphere.* **160**, 134–140 (2016).
- 18. Z. Wang, T. Horseman, A. P. Straub, N. Y. Yip, D. Li, M. Elimelech, S. Lin, Pathways and
- challenges for efficient solar-thermal desalination. Sci. Adv. 5, eaax0763 (2019).
- 450 19. A. Deshmukh, C. Boo, V. Karanikola, S. Lin, A. P. Straub, T. Tong, D. M. Warsinger, M.
- Elimelech, Membrane distillation at the water-energy nexus: limits, opportunities, and
- 452 challenges. *Energy Environ. Sci.* **11**, 1177–1196 (2018).
- 453 20. W. Liu, R. Wang, A. P. Straub, S. Lin, Membrane Design Criteria and Practical Viability of
- 454 Pressure-Driven Distillation. *Environ. Sci. Technol.* **57**, 2129–2137 (2023).
- 455 21. K. P. Lopez, R. Wang, E. A. Hjelvik, S. Lin, A. P. Straub, Toward a universal framework
- for evaluating transport resistances and driving forces in membrane-based desalination
- 457 processes. Sci. Adv. 9, eade0413 (2023).
- 458 22. J. Lee, R. Karnik, Desalination of water by vapor-phase transport through hydrophobic
- 459 nanopores. J. Appl. Phys. **108**, 044315 (2010).
- 460 23. M. Khayet, Membranes and theoretical modeling of membrane distillation: A review. Adv.
- 461 *Colloid Interface Sci.* **164**, 56–88 (2011).
- 462 24. A. P. Straub, N. Y. Yip, S. Lin, J. Lee, M. Elimelech, Harvesting low-grade heat energy
- using thermo-osmotic vapour transport through nanoporous membranes. *Nat. Energy.* 1,
- 464 16090 (2016).
- 465 25. L. Eykens, K. De Sitter, C. Dotremont, L. Pinoy, B. Van der Bruggen, Characterization and
- 466 performance evaluation of commercially available hydrophobic membranes for direct
- contact membrane distillation. *Desalination*. **392**, 63–73 (2016).
- 468 26. M. Khayet, A. O. Imdakm, T. Matsuura, Monte Carlo simulation and experimental heat and
- mass transfer in direct contact membrane distillation. *Int. J. Heat Mass Transf.* **53**, 1249–
- 470 1259 (2010).

- 27. J. Zuo, S. Bonyadi, T.-S. Chung, Exploring the potential of commercial polyethylene 471 membranes for desalination by membrane distillation. J. Membr. Sci. 497, 239–247 (2016). 472
- 28. L. F. Dumée, K. Sears, J. Schütz, N. Finn, C. Huynh, S. Hawkins, M. Duke, S. Gray, 473
- Characterization and evaluation of carbon nanotube Bucky-Paper membranes for direct 474
- contact membrane distillation. J. Membr. Sci. 351, 36–43 (2010). 475
- 29. H. Ke, E. Feldman, P. Guzman, J. Cole, Q. Wei, B. Chu, A. Alkhudhiri, R. Alrasheed, B. S. 476
- Hsiao, Electrospun polystyrene nanofibrous membranes for direct contact membrane 477
- distillation. J. Membr. Sci. 515, 86-97 (2016). 478
- 479 30. J. Pan, C. Xiao, Q. Huang, H. Liu, J. Hu, ECTFE porous membranes with conveniently controlled microstructures for vacuum membrane distillation. J. Mater. Chem. A. 3, 23549– 480
- 23559 (2015). 481
- 31. O. Labban, C. Liu, T. H. Chong, J. H. Lienhard, Relating transport modeling to 482 nanofiltration membrane fabrication: Navigating the permeability-selectivity trade-off in 483 desalination pretreatment. J. Membr. Sci. 554, 26–38 (2018). 484
- 32. G. M. Geise, H. B. Park, A. C. Sagle, B. D. Freeman, J. E. McGrath, Water permeability 485 and water/salt selectivity tradeoff in polymers for desalination. J. Membr. Sci. 369, 130– 486 138 (2011). 487
- 33. J. R. Werber, A. Deshmukh, M. Elimelech, The Critical Need for Increased Selectivity, Not 488 Increased Water Permeability, for Desalination Membranes. Environ. Sci. Technol. Lett. 3, 489 112–120 (2016). 490
- 491 34. A. Deshmukh, J. Lee, Membrane desalination performance governed by molecular reflection at the liquid-vapor interface. Int. J. Heat Mass Transf. 140, 1006–1022 (2019). 492
- 35. F. Restagno, L. Bocquet, T. Biben, Metastability and Nucleation in Capillary Condensation. 493 Phys. Rev. Lett. 84, 2433-2436 (2000). 494
- 36. J. Lee, T. Laoui, R. Karnik, Nanofluidic transport governed by the liquid/vapour interface. 495 *Nat. Nanotechnol.* **9**, 317–323 (2014). 496
- 37. P. M. Winkler, A. Vrtala, P. E. Wagner, M. Kulmala, K. E. J. Lehtinen, T. Vesala, Mass 497 and Thermal Accommodation during Gas-Liquid Condensation of Water. Phys. Rev. Lett. 498 **93**, 075701 (2004). 499
- 38. W. Chen, S. Chen, T. Liang, Q. Zhang, Z. Fan, H. Yin, K.-W. Huang, X. Zhang, Z. Lai, P. 500 Sheng, High-flux water desalination with interfacial salt sieving effect in nanoporous 501 carbon composite membranes. Nat. Nanotechnol. 13, 345–350 (2018). 502
- 39. H. Hyung, J.-H. Kim, A mechanistic study on boron rejection by sea water reverse osmosis 503 membranes. J. Membr. Sci. 286, 269–278 (2006). 504

- 505 40. M. T. Pickett, L. B. Roberson, J. L. Calabria, T. J. Bullard, G. Turner, D. H. Yeh, 506 Regenerative water purification for space applications: Needs, challenges, and technologies
- towards "closing the loop." *Life Sci. Space Res.* **24**, 64–82 (2020).
- 41. T. Merle, W. Pronk, U. von Gunten, MEMBRO3X, a Novel Combination of a Membrane
- Contactor with Advanced Oxidation (O3/H2O2) for Simultaneous Micropollutant
- Abatement and Bromate Minimization. *Environ. Sci. Technol. Lett.* **4**, 180–185 (2017).
- 511 42. S. Ling, Z. Qin, C. Li, W. Huang, D. L. Kaplan, M. J. Buehler, Polymorphic regenerated silk fibers assembled through bioinspired spinning. *Nat. Commun.* **8**, 1387 (2017).
- 43. Y.-H. Chuang, A. Y.-C. Lin, X. Wang, H. Tung, The contribution of dissolved organic
- nitrogen and chloramines to nitrogenous disinfection byproduct formation from natural
- organic matter. Water Res. 47, 1308–1316 (2013).
- 516 44. W. Wang, X. Du, H. Vahabi, S. Zhao, Y. Yin, A. K. Kota, T. Tong, Trade-off in membrane distillation with monolithic omniphobic membranes. *Nat. Commun.* **10**, 3220 (2019).
- 518 45. Z. Wang, S. Lin, Membrane fouling and wetting in membrane distillation and their mitigation by novel membranes with special wettability. *Water Res.* **112**, 38–47 (2017).
- 520 46. F. Zhao, X. Zhou, Y. Shi, X. Qian, M. Alexander, X. Zhao, S. Mendez, R. Yang, L. Qu, G.
- Yu, Highly efficient solar vapour generation via hierarchically nanostructured gels. *Nat.*
- *Nanotechnol.* **13**, 489–495 (2018).
- 47. P. L. Barclay, J. R. Lukes, Curvature Dependence of the Mass Accommodation Coefficient.
- 524 *Langmuir.* **35**, 6196–6202 (2019).
- 48. L. Chen, J. Ma, Y. Huang, M. Dai, X. Li, Optimization of a colorimetric method to
- determine trace urea in seawater. *Limnol. Oceanogr. Methods.* **13**, 303–311 (2015).
- 49. R. Bernstein, S. Belfer, V. Freger, Toward Improved Boron Removal in RO by Membrane
- Modification: Feasibility and Challenges. *Environ. Sci. Technol.* **45**, 3613–3620 (2011).
- 529 50. M. E. Huang, S. Huang, D. L. McCurry, Re-Examining the Role of Dichloramine in High-
- Yield N-Nitrosodimethylamine Formation from N,N-Dimethyl-α-arylamines. *Environ. Sci.*
- 531 *Technol. Lett.* **5**, 154–159 (2018).
- 532 51. J. Lee, A. P. Straub, M. Elimelech, Vapor-gap membranes for highly selective osmotically
- driven desalination. *J. Membr. Sci.* **555**, 407–417 (2018).
- 534 52. G. Vaartstra, Z. Lu, J. H. Lienhard, E. N. Wang, Revisiting the Schrage Equation for
- Kinetically Limited Evaporation and Condensation. J. Heat Transf. 144, 080802 (2022).
- 53. I. W. Eames, N. J. Marr, H. Sabir, The evaporation coefficient of water: a review. *Int. J.*
- 537 *Heat Mass Transf.* **40**, 2963–2973 (1997).

- 538 54. A. S. Berman, Free Molecule Transmission Probabilities. *J. Appl. Phys.* **36**, 3356–3356 (1965).
- 540 55. Z. Yang, H. Guo, C. Y. Tang, The upper bound of thin-film composite (TFC) polyamide membranes for desalination. *J. Membr. Sci.* **590**, 117297 (2019).
- 542 56. X. Chen, C. Boo, N. Y. Yip, Influence of Solute Molecular Diameter on Permeability-
- Selectivity Tradeoff of Thin-Film Composite Polyamide Membranes in Aqueous
- Separations. *Water Res.* **201**, 117311 (2021).
- 545 57. N. Y. Yip, M. Elimelech, Performance Limiting Effects in Power Generation from Salinity Gradients by Pressure Retarded Osmosis. *Environ. Sci. Technol.* **45**, 10273–10282 (2011).
- 58. B. Abad, J. Maiz, M. Martin-Gonzalez, Rules to Determine Thermal Conductivity and Density of Anodic Aluminum Oxide (AAO) Membranes. *J. Phys. Chem. C.* **120**, 5361–549 5370 (2016).
- 550 59. Y. Chung, D. Park, H. Kim, S.-E. Nam, S. Kang, Novel method for the facile control of molecular weight cut-off (MWCO) of ceramic membranes. *Water Res.* **215**, 118268 (2022).
- 552 60. B. Jung, C. Y. Kim, S. Jiao, U. Rao, A. V. Dudchenko, J. Tester, D. Jassby, Enhancing 553 boron rejection on electrically conducting reverse osmosis membranes through local 554 electrochemical pH modification. *Desalination*. **476**, 114212 (2020).
- 61. A. Alkhudhiri, N. Darwish, N. Hilal, Membrane distillation: A comprehensive review. Desalination. **287**, 2–18 (2012).
- 62. R. Verbeke, V. Gómez, I. F. J. Vankelecom, Chlorine-resistance of reverse osmosis (RO) polyamide membranes. *Prog. Polym. Sci.* **72**, 1–15 (2017).
- 63. R. Wang, S. Lin, Pore model for nanofiltration: History, theoretical framework, key predictions, limitations, and prospects. *J. Membr. Sci.* **620**, 118809 (2021).
- 561 64. S. Lee, A. P. Straub, Analysis of Volatile and Semivolatile Organic Compound Transport in Membrane Distillation Modules. *ACS EST Eng.* **2**, 1188–1199 (2022).

### Acknowledgements

- We would like to thank the Colorado Shared Instrumentation in Nanofabrication and
- 564 Characterization Laboratory for assistance with SEM and the University of Colorado Boulder
- Department of Chemistry for assistance with the FTIR analysis. We are grateful to Dr. Dmitri
- Routkevitch at InRedox, Dr. Lucas McIntosh at 3M, and Dr. Uwe Beuscher at Gore for helpful
- discussions on membrane design and testing.
- Funding: The authors acknowledge financial support from Bureau of Reclamation, Department
- of Interior, via DWPR Agreement R22AC00425, and support received from the National Science

- Foundation under Award Number CBET 2227273. The authors also acknowledge support from
- 571 the National Science Foundation (NSF) Industry/University Cooperative Research Center for
- Membrane Science, Engineering and Technology (MAST) at the University of Colorado Boulder
- 573 (UCB, award number, IIP 1624602). D.T.N acknowledges support from the American Water
- Works Association for the 2021 Larson Aquatic Research Support Scholarship and the American
- Membrane Technology Association and U.S. Bureau of Reclamation for the 2020 Fellowship.
- 576 K.P.L acknowledges support from the National Aeronautics and Space Administration (NASA)
- 577 Space Technology Graduate Research Opportunity (NSTGRO) fellowship.
- Author contributions: D.T.N and A.P.S conceived the project, developed the process, and
- designed the experiments. D.T.N conducted membrane fabrication, material characterization,
- sample analysis, and transport and selectivity measurements. S.L and D.T.N conducted the
- transport modeling. D.T.N and K.L conducted limit of water permeability analysis. A.P.S and
- 582 D.T.N co-wrote the manuscript. All authors contributed to data analysis, discussed the results, and
- 583 commented on the manuscript.
- Competing interests: Authors declare that they have no competing interests.
- Data and materials availability: All data are available in the main text or the Supplementary
- 586 Materials.